Computationally efficient model to predict the evolution in the thermal field in the EB-PBF and LP-DED processes

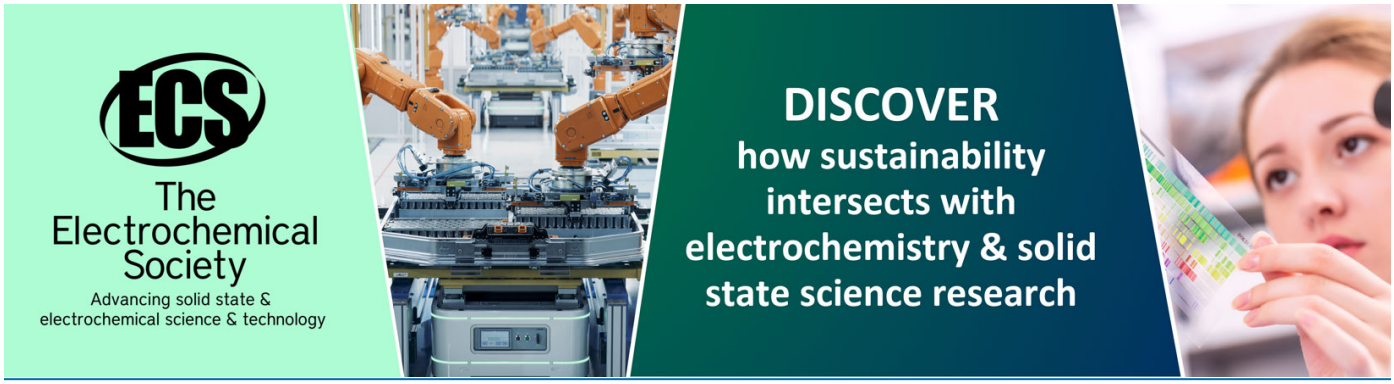

Computationally efficient model to predict the evolution in the thermal field in the EB-PBF and LP-DED processes

P Pourabdollah[1,2], F Farhang Mehr[1], S L Cockcroft[1] and D M Maijer[1]

[1] Department of Materials Engineering, University of British Columbia, 6350 Stores Rd, Vancouver, BC V6T 1Z4, Canada

[2] Corresponding author, E-mail address: pegah.pourabdollah@ubc.ca

Abstract. Understanding the development of a number of defects found in components fabricated by the metal Additive Manufacturing (AM) processes requires an understanding of the evolution in the thermal field within the component at both the macro- and meso-scales. As a first step, in this work, the agglomeration method was used in combination with a time-averaged input of energy to simulate the macro-scale evolution in temperature. Two example processes: 1) laser-based powder-fed directed energy deposition; and 2) electron beam powder bed fusion, are used to demonstrate the modelling methodology. The approach employed focuses on ensuring the conservation of heat and is applied using ABAQUS. The two applications have been validated by comparing the predicted thermal behaviour with process-derived data. The results indicate that this method is an efficient strategy to predict the thermal field at the scale of the component being fabricated.

1. Introduction

Additive Manufacturing (AM) is an advanced manufacturing method for producing components in which the feedstock material is consolidated into a metallic part in a layer-by-layer fashion [1]. The benefits of fabricating parts via AM include: the ability to produce geometrically complex near-net-shape structures; increased design flexibility; reduced part counts by reducing the need to assemble multiple components; and minimization of subtractive machining and material waste. For these reasons, AM is growing in acceptance as an alternative method for producing components for automotive, aerospace, medical, and energy applications [2,3]. However, despite these benefits, several challenges are associated with this process, including the high cost of the feedstock material in powder-based additive technologies, low productivity, porosity, surface roughness, and the development of residual stresses in the final component [4–6].

Metal AM processes include a wide range of methods, including Electron Beam Melting (EBM), Directed Energy Deposition (DED) and Selected Laser Melting (SLM). These AM techniques are based on selective melt/sintering of the build material, which may be powder or wire, using an intense, focused heat source. In these processes, the heat sources, such as an electron beam or laser, are rapidly moved over regions on a given layer consistent with the geometry of the part being fabricated [3,7,8].

In AM processes, large thermal stresses develop due to the temperature gradients associated with the rapidly moving intense heat source. Additionally, stresses may develop due to the thermal strain mismatch between the deposited material and the substrate or build plate. These strains can lead to residual stresses and component distortion. The post-fabrication removal from the substrate or the removal of support structures can also result in further deformation [9–11]. Predicting an accurate

thermal history in the components fabricated by the AM processes at the macro-scale is crucial to estimating the Type-1 residual stresses, which are the macro-scale residual stresses responsible for component distortion. Various studies have been conducted to predict the temperature field and its effect during the AM processes [12–14].

Modelling the part-scale thermal field in melt-sintering AM processes is computationally intensive as it involves transient heat transfer over two significantly different time and length scales [10,15]. To facilitate practical AM process simulation, various studies have explored different techniques to reduce computational time. For instance, some researchers have used the agglomeration method, in which several physical deposition layers are lumped into one computational layer [16–18]. Another technique to reduce the computational time is the flash heating method, in which an equivalent uniform heat source is applied to each layer instead of modelling the precise details of the heat source-material interaction [19, 20]. Although the agglomeration and flash heating methods can reduce the computational cost, these methods cannot capture the thermal behaviour at high spatial and temporal resolution during the process – e.g., the size and location of the melt pool cannot be predicted.

In this work, the macro-scale evolution in temperature was simulated using a combination of the agglomeration and flash heat methods. Two applications were used to illustrate the analysis methodology: a Laser-based, Powder-fed Direct Energy Deposition (LP-DED) process and an Electron Beam Powder Bed Fusion (EB-PBF) process. The novelty of the approach presented is that it is formulated around the principle of heat conservation. In the LP-DED process, the time-averaged input of energy is corrected for the enthalpy of the deposited material. In the EB-PBF process, the time-averaged input of energy is corrected for the enthalpy of the powder following the powder layer preheat. The two applications were validated by comparing the predicted thermal behaviour to the experimentally derived data. The results show that this approach effectively predicts the thermal field at the part scale.

2. Model development

For the two applications, LP-DED and EB-PBF, separate 3D, transient thermal models were developed in ABAQUS[1].

2.1. Geometry, mesh and element activation

Figure 1 shows the computational domain in various views (a)-(c), which includes the baseplate, the component geometry and the fixturing used for the LP-DED process. The figure also includes mesh (d), which contained 12,621 nodes and 9208 elements. The part was partitioned into 11 super layers. Each super layer represents the agglomeration of 4 physical process layers. The thickness of each super layer is 1.96 mm = 4 layers × 0.49 mm/layer [21].

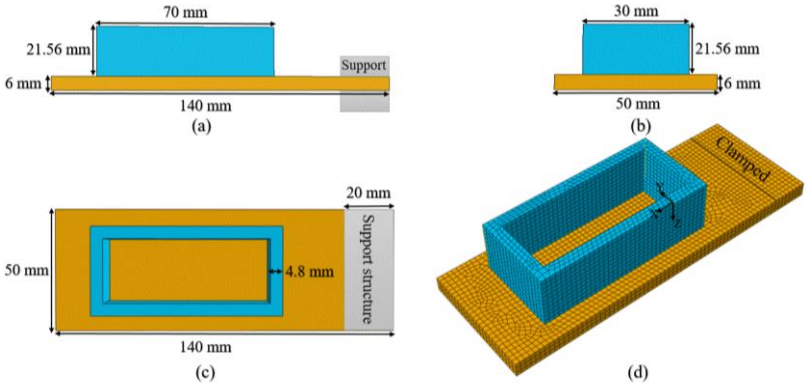

Figure 1. The dimensioned 2D drawing of the geometry fabricated with LP-DED (a) front view, (b) side view, (c) top view and (d) the analysis mesh [21].

[1] ABAQUS is the trademark for Dassault Systèmes.

Figure 2 shows the computational domain, including the part (a), baseplate and surrounding powder bed geometries (b) and mesh (c) for the EB-PBF process. The mesh contained 52,344 nodes and 44,700 elements. The powder bed and part were partitioned into 16 super layers. Each super layer represents the agglomeration of 6 physical process layers. The thickness of each super layer is 0.54 mm = 6 layers × 0.09 mm/layer.

For both applications, the number of physical layers per super layer was determined from a sensitivity analysis in which a balance was achieved between computational efficiency and accuracy. The deactivate/activate method was used to implement the sequential deposition of the layers. In this method, all elements in the domain are generated in the model before starting the analysis. Then, as the analysis starts, all elements of the part and/or powder bed are deactivated. During the analysis, the super layers of elements associated with the part and surrounding powder are then reactivated in a step-by-step sequence at the appropriate time.

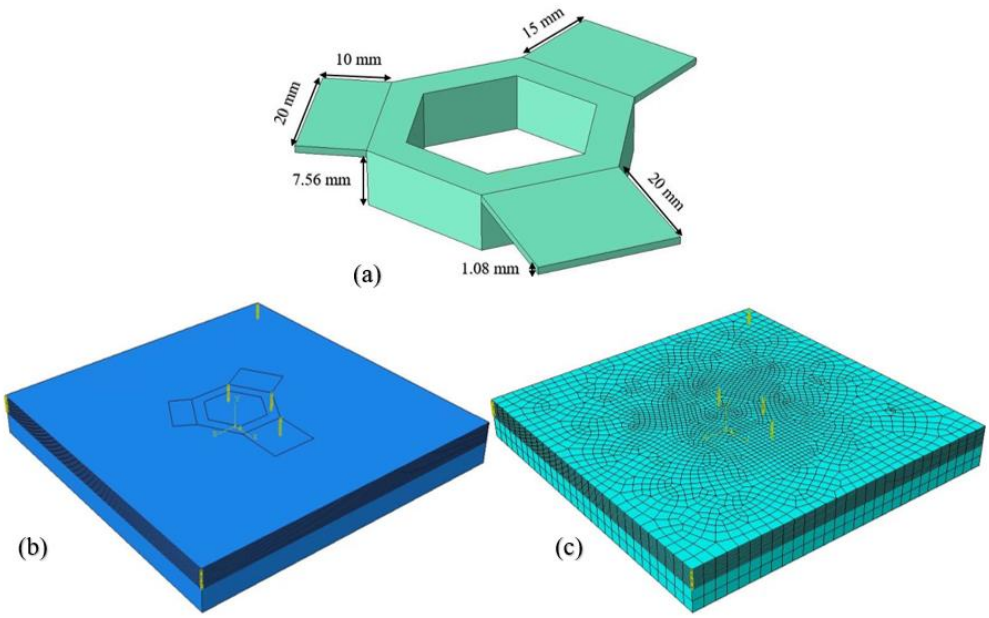

Figure 2. (a) fabricated component, (b) 3D computational domain including powder bed, baseplate, and component, and (c) mesh topography.

2.2. Thermal analysis

The governing equation for 3D transient heat balance is given in Eq. 1.

$$\frac{\partial}{\partial x}\left(k\frac{\partial T}{\partial x}\right)+\frac{\partial}{\partial y}\left(k\frac{\partial T}{\partial y}\right)+\frac{\partial}{\partial z}\left(k\frac{\partial T}{\partial z}\right)+\dot{Q}=\frac{\partial(\rho C_P T)}{\partial t} \quad (1)$$

where k is the thermal conductivity (W m^{-1} K^{-1}), T is the temperature (K), $\dot{Q}$ is the volumetric heat input rate (W m^{-3}), ρ is the density (kg m^{-3}), C_p is the specific heat capacity (J kg^{-1} K^{-1}), t is time (s), and x, y, z are the coordinates (m).

A time-averaged volumetric heat input methodology was implemented for each computational layer over the time associated with the deposition of the super layer. Thus, for example, in the EB-PBF process, the approach does not account for the process-related steps that would occur on a per powder layer basis – i.e., powder deposition, preheat-1, contouring, hatching and preheat-2 are not explicitly considered. Rather the timing of each is accounted for in the determination of the time-averaged energy input over the six process layers that are included in a single layer of elements.

In the approach used for both applications, the new layer of elements being added is activated at an elevated temperature. There are several reasons for doing this. In the LP-DED process, a portion of the laser energy is consumed by the powder stream entering the beam leading to this material being deposited at an elevated temperature. In the analysis of the LP-DED process, an assumption is made for the resulting temperature of the deposited material. In the case of the EB-PBF process, following the deposition of a powder layer, the new layer is preheated to a target temperature, which is reported to be ~950 °C, prior to beam contouring and hatching. In the context of the layer agglomeration method, these temperatures form the initial temperature for activation of the element layer, which must be considered in the overall system energy balance. This approach also benefits computational efficiency, and there are implications associated with capturing the generation of plastic strain at elevated temperatures, which are beyond the scope of this manuscript.

To correct the heat input for the enthalpy associated with activating the elements at the elevated temperature, the expressions shown in Eqs 2 and 3 are used.

$$\dot{Q}_{enthalpy} = \rho\big(C_p(T_{act} - T_{ref}\big)\frac{1}{t_{total}} \tag{2}$$

where ρ is the density (kg m^{-3}), C_p is the heat capacity (J kg^{-1} K^{-1}), T_{act} is the activation temperature of the new layer of elements (°C), T_{ref} is the reference temperature (°C) and t_{total} is the total time taken to process a super layer of elements.

$$\dot{Q}_{time\_avg} = \eta\dot{Q}_{beam}\frac{t_{beam}}{t_{total}} - \dot{Q}_{enthalpy} \tag{3}$$

where $\dot{Q}_{time\_avg}$ is the net time-averaged volumetric heat input rate (W m^{-3}) applied to each super layer, t_{beam} is the total time the beam is on during the deposition of the powder layers in a super layer, t_{total} is the total time taken to process powder layers in a super layer, $\dot{Q}_{beam}$ is the heat input rate (W m^{-3}), η is the absorptivity of the material being heated. In the case of the LP-DED process, the efficiency of heating, η, is set to 0.37, and for the EB-PBF process, it is set to 0.9.

For the LP-DED process, the beam power, $\dot{Q}_{beam}$, was 1500 W [18]. For the EB-PBF process, separate and time-varying heat inputs were applied to the component and the surrounding powder bed within each layer following activation. The energy input rates were extracted from data obtained from an ARCAM Q20Plus system, including the variation of voltage and current with time. The ARCAM Q20Plus system uses a series of different settings (including beam power, speed and focus) for what are referred to as process themes. The heat input for each process layer of the component is the sum of the energies from preheat-1, contour, hatch, and preheat-2 themes, whereas the heat input for the surrounding powder is the sum of the energies from preheat-1 and preheat-2 themes. The calculated heat inputs for each layer were then averaged over every six layers in the component and surrounding powder bed to calculate the heat input for each super layer of the component and surrounding powder bed in the analysis. The resulting time-averaged heat inputs, $\dot{Q}_{beam}$, are shown in Figure 3.

Referring to Figure 3, for the first few layers (up to the 12th layer), the time-averaged heat input increases due to the continuous application of the preheat-2 theme. The time-averaged heat input then decreases and oscillates around a constant value from the 12th to the 75th layer due to a reduction in the frequency of use of the preheat-2 theme. Toward the end of the build, the time-averaged heat input increases again during the deposition of the layers (84th layer to 96th layer) associated with the fabrication of the platforms on the component.

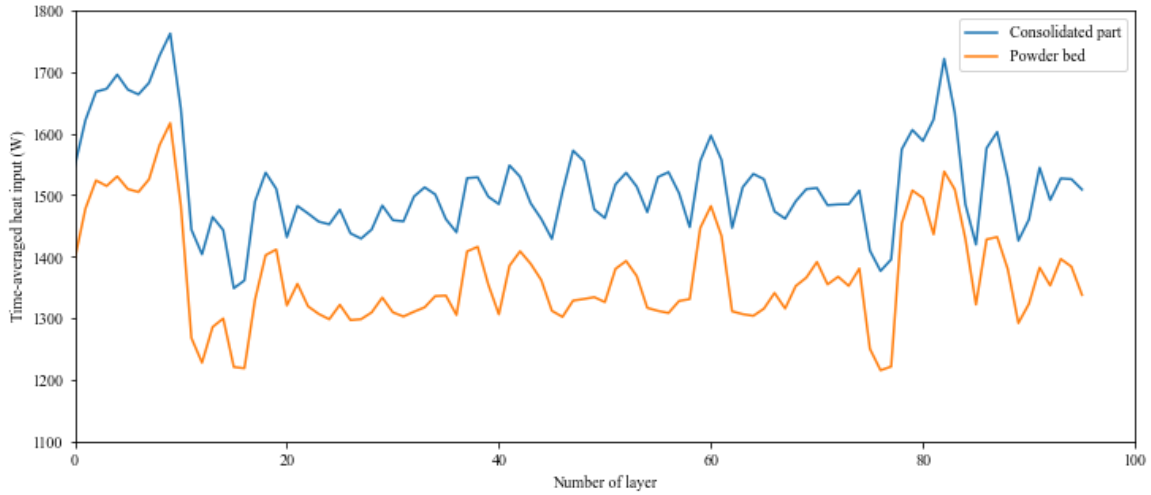

Figure 3. The time-averaged energy input for each layer of the component and surrounding powder bed.

2.2.1. Boundary conditions

During the LP-DED process, heat loss occurs via conduction to the baseplate, convection due to the flow of inert gas on the free surfaces (captured using a heat transfer coefficient of 5 W m^{-2} K^{-1}) and radiation from all the free surfaces on the component and baseplate to the surrounding environment. The baseplate also loses heat by conduction to the support structure that the baseplate is clamped to (refer to Figure 1). The ambient temperature was set to 25 °C. Conductive heat loss between the baseplate and the fixture was also defined via an increased heat transfer coefficient of 50 W m^{-2} K^{-1} [18].

During the EB-PBF process, heat loss occurs by conduction to the baseplate/surrounding powder bed and radiation from the top surface of the domain. The surface emissivity was set to 0.769 [22], and the ambient temperature was set to 350 °C. A contact boundary condition was defined to consider the conductive heat loss between the component and powder bed with a thermal conductance of 0.4 W m^{-2} K^{-1}.

2.2.2. Initial conditions

For the LP-DED process, the initial baseplate temperature was set to 25 °C. In addition, the activation temperature of the deposited material was set to 2200 °C [21]. For the EB-PBF process, the initial temperature of the baseplate was set to 750 °C, and the activation temperature of the deposited material for the component and powder bed was set to 950 °C.

2.3. Material properties

For the LP-DED process, the temperature-dependent thermo-physical properties of consolidated Ti-6Al-4V (Ti64) were used for both the baseplate and rectangular component [21]. For the EB-PBF process, the temperature-dependent thermo-physical properties of consolidated Ti64 were used for the component. The powder was treated as a bulk material, and the density and thermal conductivity were reduced by a factor of 0.5 relatives to bulk Ti64 to account for the void space between the discrete particles. The temperature-dependent thermo-physical properties of 304L stainless steel were used for the baseplate [23].

3. Results and discussion

The simulation results for both applications were validated by comparing the predicted thermal behaviour with process-derived data. Figure 4 shows a comparison between the predicted thermal history of the baseplate in the LP-DED process and the in-situ experimental measurements at two

locations on the bottom surface of the baseplate reported by Lu *et al.* [18]. As can be seen, there is relatively good agreement between the simulated and measured thermal history of the baseplate, with a maximum error of approximately 10%. Furthermore, the execution time was less than 10 min using 12, 2.33 GHz, Intel Quad-core CPUs.

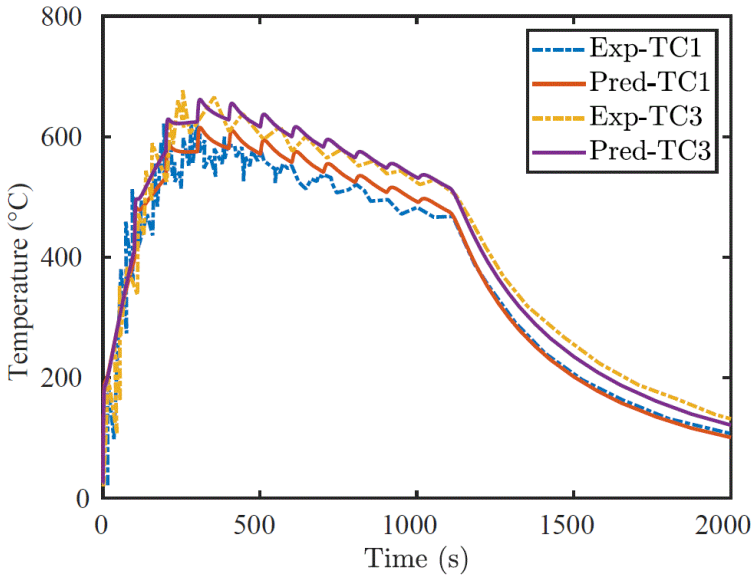

Figure 4. Measured [18] and predicted thermal history at two locations on the bottom surface of the baseplate [21].

Referring to Figure 4, the temperature of the baseplate increases rapidly during the addition of the first three super layers. The temperature then gradually reduces as the deposition continues. This reduction in temperature is due to the increased distance (and resistance to conduction) from the thermocouple locations to the layer of material being deposited. Finally, as the deposition of all layers is complete, the baseplate cools down. During the addition of each layer, it can also be seen that the predicted and measured thermal behaviour both show periodic, quick rises followed by gradual falls in temperature. This behaviour is associated with the deposition of hot material in a layer-by-layer process.

Figure 5 shows a qualitative comparison between the simulated temperature contour and a grey-scale image obtained by the ARCAM Q20Plus EB-PBF system during the manufacturing process. The image was captured after the deposition of all layers of the component (96 physical process layers, which corresponds to 16 super layers in the model). As can be seen, the model can qualitatively predict the difference in temperature observed between the inner support structure and the platforms. The higher temperature observed in the platforms is due to a combination of the increased area over which heat is input and their fabrication on un-consolidated powder resulting in a reduced path for conduction to the build plate. The execution time was approximately 2 hours using 12, 2.33 GHz, Intel Quad-core CPUs. Notes: 1) calibration of the grey-scale image from the ARCAM camera to temperature is ongoing; 2) the ABAQUS grey-scale shown is linear in temperature and must be corrected.

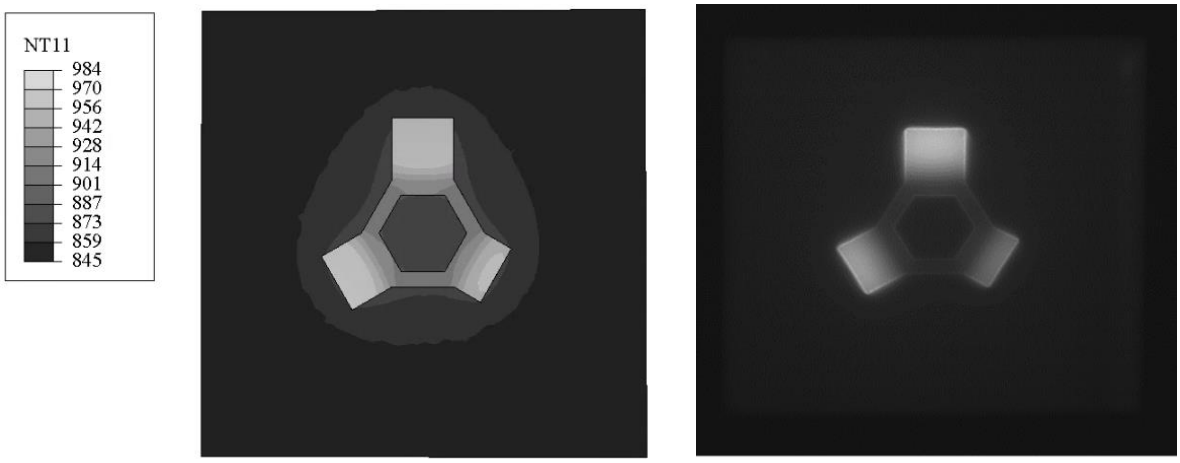

(a) (b)

Figure 5. A qualitative comparison between the predicted grey-scale temperature contour (a) and an image captured by the ARCAM Q20Plus EB-BPF system (b) at the end of the deposition of all layers.

As a second means of assessing the validity of the model predictions qualitatively, a comparison between a colour image captured during the EB-PBF manufacturing process and the predicted temperature contour is shown in Figure 6. Again, this comparison shows relatively good qualitative agreement between the model predictions and the process conditions.

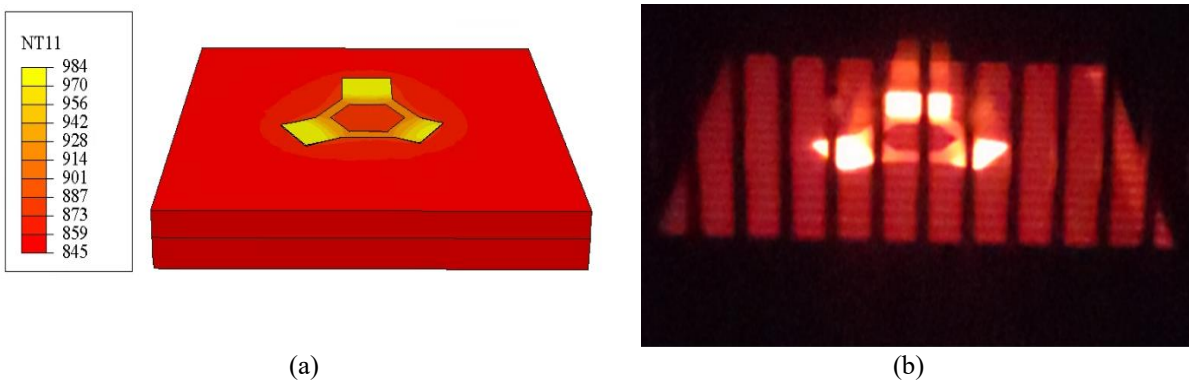

(a) (b)

Figure 6. A qualitative comparison between the simulated temperature contour (a) and an image captured during the EB-PBF manufacturing process (b).

4. Summary and conclusions

The accurate prediction of the temperature distribution at the macro-scale and its evolution during component fabrication in the metal AM processes is essential to be able to predict important phenomena developing at the meso-scale. These phenomena include pore formation, plastic strain accumulation, microstructure, and the evaporative losses of volatile alloy constituents. This work demonstrates a modelling methodology using the agglomeration method in combination with time-averaged heat input that is relatively fast to run and efficient. The method was implemented to simulate two process applications: an LP-DED process and an EB-PBF process. The conservation of heat was applied in the method employed in ABAQUS. The predicted thermal behaviour for both applications was compared against the process-derived data to validate the model. The results showed good quantitative agreement

between predicted and experimental data in the case of the LP-DED process and good qualitative agreement in the case of the EB-PBF process.

5. Acknowledgement

The authors would like to acknowledge the NSERC Network for Holistic Innovation in Additive Manufacturing (HI-AM) for the financial support of this project.

References

[1] Gibson I, Rosen D, Stucker B. Additive manufacturing technologies: 3D printing, rapid prototyping, and direct digital manufacturing, second edition. 2015. https://doi.org/10.1007/978-1-4939-2113-3.

[2] DebRoy T, Wei HL, Zuback JS, Mukherjee T, Elmer JW, Milewski JO, et al. Additive manufacturing of metallic components – Process, structure and properties. Prog Mater Sci 2018;92. https://doi.org/10.1016/j.pmatsci.2017.10.001.

[3] Herzog D, Seyda V, Wycisk E, Emmelmann C. Additive manufacturing of metals. Acta Mater 2016;117. https://doi.org/10.1016/j.actamat.2016.07.019.

[4] Li C, Liu JF, Fang XY, Guo YB. Efficient predictive model of part distortion and residual stress in selective laser melting. Addit Manuf 2017;17. https://doi.org/10.1016/j.addma.2017.08.014.

[5] Aboulkhair NT, Everitt NM, Ashcroft I, Tuck C. Reducing porosity in AlSi10Mg parts processed by selective laser melting. Addit Manuf 2014;1. https://doi.org/10.1016/j.addma.2014.08.001.

[6] King WE, Barth HD, Castillo VM, Gallegos GF, Gibbs JW, Hahn DE, et al. Observation of keyhole-mode laser melting in laser powder-bed fusion additive manufacturing. J Mater Process Technol 2014;214. https://doi.org/10.1016/j.jmatprotec.2014.06.005.

[7] Körner C. Additive manufacturing of metallic components by selective electron beam melting - A review. International Materials Reviews 2016;61. https://doi.org/10.1080/09506608.2016.1176289.

[8] Li Y, Zhou K, Tan P, Tor SB, Chua CK, Leong KF. Modeling temperature and residual stress fields in selective laser melting. Int J Mech Sci 2018;136. https://doi.org/10.1016/j.ijmecsci.2017.12.001.

[9] Liang X, Cheng L, Chen Q, Yang Q, To AC. A modified method for estimating inherent strains from detailed process simulation for fast residual distortion prediction of single-walled structures fabricated by directed energy deposition. Addit Manuf 2018;23. https://doi.org/10.1016/j.addma.2018.08.029.

[10] Mukherjee T, Zhang W, DebRoy T. An improved prediction of residual stresses and distortion in additive manufacturing. Comput Mater Sci 2017;126. https://doi.org/10.1016/j.commatsci.2016.10.003.

[11] DebRoy T, Wei HL, Zuback JS, Mukherjee T, Elmer JW, Milewski JO, et al. Additive manufacturing of metallic components – Process, structure and properties. Prog Mater Sci 2018;92:112–224. https://doi.org/10.1016/J.PMATSCI.2017.10.001.

[12] Cao X, Ayalew B. Control-oriented MIMO modeling of laser-aided powder deposition processes. Proceedings of the American Control Conference 2015;2015-July:3637–42. https://doi.org/10.1109/ACC.2015.7171895.

[13] Toyserkani E, Khajepour A, Corbin S. 3-D finite element modeling of laser cladding by powder injection: effects of laser pulse shaping on the process. Opt Lasers Eng 2004;41:849–67. https://doi.org/10.1016/S0143-8166(03)00063-0.

[14] Hoadley AFA, Rappaz M. A thermal model of laser cladding by powder injection. Metallurgical Transactions B 1992 23:5 1992;23:631–42. https://doi.org/10.1007/BF02649723.
[15] Vastola G, Zhang G, Pei QX, Zhang YW. Controlling of residual stress in additive manufacturing of Ti6Al4V by finite element modeling. Addit Manuf 2016;12:231–9. https://doi.org/10.1016/J.ADDMA.2016.05.010.
[16] Ganeriwala RK, Strantza M, King WE, Clausen B, Phan TQ, Levine LE, et al. Evaluation of a thermomechanical model for prediction of residual stress during laser powder bed fusion of Ti-6Al-4V. Addit Manuf 2019;27. https://doi.org/10.1016/j.addma.2019.03.034.
[17] Hodge NE, Ferencz RM, Vignes RM. Experimental comparison of residual stresses for a thermomechanical model for the simulation of selective laser melting. Addit Manuf 2016;12. https://doi.org/10.1016/j.addma.2016.05.011.
[18] Lu X, Lin X, Chiumenti M, Cervera M, Hu Y, Ji X, et al. Residual stress and distortion of rectangular and S-shaped Ti-6Al-4V parts by Directed Energy Deposition: Modelling and experimental calibration. Addit Manuf 2019;26:166–79. https://doi.org/10.1016/j.addma.2019.02.001.
[19] Kiran A, Hodek J, Vavřík J, Urbánek M, Džugan J. Numerical simulation development and computational optimization for directed energy deposition additive manufacturing process. Materials 2020;13. https://doi.org/10.3390/ma13112666.
[20] Wang J, Zhang J, Liang L, Huang A, Yang G, Pang S. A line-based flash heating method for numerical modeling and prediction of directed energy deposition manufacturing process. J Manuf Process 2022;73:822–38. https://doi.org/10.1016/j.jmapro.2021.11.041.
[21] Pourabdollah P, Farhang Mehr F, Maijer DM, Cockcroft SL. A novel approach for the numerical analysis of in situ distortion in a component made by the directed energy deposition additive manufacturing process. The International Journal of Advanced Manufacturing Technology 2022 2022:1–14. https://doi.org/10.1007/S00170-022-10562-Z.
[22] Coppa P, Consorti A. Normal emissivity of samples surrounded by surfaces at diverse temperatures. Measurement 2005;38:124–31. https://doi.org/10.1016/J.MEASUREMENT.2005.05.001.
[23] ASM Handbook Volume 22B: Metals Process Simulation - ASM International n.d. https://www.asminternational.org/search/-/journal_content/56/10192/05281G/PUBLICATION (accessed December 18, 2022).